



# End effect correction for orthogonal small strain oscillatory shear in a rotational shear rheometer

Ran Tao<sup>1,2</sup> · Aaron M. Forster<sup>1</sup>

Received: 2 October 2019 / Revised: 5 December 2019 / Accepted: 23 December 2019

© This is a U.S. government work and not under copyright protection in the U.S.; foreign copyright protection may apply 2020

## Abstract

The orthogonal superposition (OSP) technique is advantageous for measuring structural dynamics in complex fluids subjected to a primary shear flow. This technique superimposes a small-amplitude oscillation orthogonal to a primary shear flow to measure the real and imaginary components of the complex shear modulus. The commercial availability of OSP geometries and bi-axial transducers is expected to increase its adoption as a more routine rheological technique. It is important to understand calibration procedures and the influence of intrinsic inhomogeneous flow fields, residual pumping flow effects, and boundary forces at the leading edges of the geometry components on experimental error and measurement uncertainty. In this work, we perform calibration measurements of viscosity standards on a commercial shear rheometer using a double-wall concentric cylinder geometry. Newtonian calibration fluids with viscosities that range from 0.01 to 331 Pa s are used to obtain the end-effect factors in primary steady shear and orthogonal oscillatory shear directions. The corrections needed for the viscosity measured in steady shear range from 16 to 21%; whereas for the orthogonal complex viscosity, the errors range from 19 to 25%. Computational fluid dynamics simulations are used to understand the relationship between the end-effect corrections, OSP flow cell, and the imposed shear flow fields. We show that approximate linear shear deformation profiles are attained, in the double gap, for both primary rotational shear and orthogonal oscillatory shear deformation, with only a slight deviation for the fluid in the vicinity of the bob ends. We also present information on the velocity, pressure, and shear rate distributions for fluid within the entire flow cell. The overestimation of the orthogonal viscosity is attributed to the pressure forces exerted on the bob end surfaces (9%) and a higher shear rate in the double gap that leads to higher viscous stresses on the bob cylindrical surfaces (8%). The Newtonian fluid field information provides a benchmark for future simulations involving non-Newtonian fluids. Additionally, the operational knowledge (i.e., consistent sample filling) and measurement window (i.e., viscosity and frequency) described within are critical for proper use of the instrument and measurement accuracy.

**Keywords** Rheology · Orthogonal superposition · Viscosity · Calibration · Newtonian fluids

---

**Electronic supplementary material** The online version of this article (<https://doi.org/10.1007/s00397-019-01185-5>) contains supplementary material, which is available to authorized users.

---

✉ Ran Tao  
ran.tao@nist.gov

✉ Aaron M. Forster  
aaron.forster@nist.gov

<sup>1</sup> Materials Measurement Science Division, National Institute of Standards and Technology, Gaithersburg, MD 20899, USA

<sup>2</sup> Department of Chemical Engineering, Texas Tech University, Lubbock, TX 79409, USA

## Introduction

The orthogonal superposition (OSP) technique, which involves superimposing a small-amplitude oscillation on a primary steady shear flow, allows for probing structural changes in complex fluids under nonlinear flow conditions. As the flow in the axial and angular directions are not coupled, the rate-dependent relaxation spectra measured in the axial direction directly interrogate flow-induced structures defined by the primary flow (Vermant et al. 1998; Yamamoto 1971). The implementation of the modern OSP geometry is the result of many decades of development. The axial deformation of a fluid was first achieved by oscillating a rod vertically in a fluid

container (Birnboim and Ferry 1961; Philippoff 1934; Smith et al. 1949). The first implementation of orthogonal flow fields was reported by Simmons (1966) utilizing an open-ended double-wall Couette (or concentric cylinder) flow cell. In such a configuration, a thin-walled cylinder performs oscillation in the axial direction within a concentric outer cylinder that contains a large reservoir which can rotate about the center axis. To achieve better instrument sensitivity, Tanner and Williams (1971) modified the device and replaced the flow cell with an annular pumping geometry, i.e., a simple Couette. In this annular pumping geometry, the fluid flow profile is a combination of linear axial shear deformation and a pressure-driven Poiseuille flow from the displacement of fluid by the closed end of the bob. Major disadvantages were readily identified, e.g., non-uniform shear rate across the annular gap and possible cavitation of the fluid. Mewis and Schoukens (1978) developed a similar instrument using a narrow gap Couette with an opening at the cup bottom to drain the fluid from the flow cell. Later, Zeegers et al. (1995) built an apparatus that employed a closed bottom double-wall Couette geometry, which required less sample volume than that of Simmons (1966) and reduced the annular pumping effect for simple Couette as used in Tanner and Williams (1971) and Mewis and Schoukens (1978). Vermant et al. (1997) utilized a hollow inner cup and a modified force rebalance transducer on a commercial rheometer to perform orthogonal superposition measurements for a wider viscosity range than previous devices. The pumping effect was minimized because the fluid, displaced by the bob, was able to flow back and forth between the annular gap and the inner cup fluid reservoir.

The development of these custom OSP devices has led to the integration of the OSP hardware and software functionality into a commercial strain-controlled ARES-G2 rheometer (Franck 2013). The normal force rebalance transducer is modified to operate as a stress-controlled rheometer, allowing the shaft to apply axial deformation and measure the axial oscillation force. The axial motion is imposed simultaneously with the motion of the rotary motor, which is able to induce an orthogonal oscillatory or steady shear in the angular direction. The commercial OSP flow cell is a double-wall concentric cylinder geometry with two annular gaps available, i.e., 0.5 mm and 1 mm. The design of the flow cell, based on the early approaches of Simmons (1966) and Zeegers et al. (1995) and a recent design of Vermant et al. (1997), is optimized to minimize pumping and reduce surface tension effects at the fluid surface by the addition of rectangular openings to the bottom of the inner cylinder and to the top of the bob. The bottom openings minimize pumping effects, and the top openings reduce surface tension effects (Franck 2013).

The OSP technique has been employed to study various structured fluids, including polymeric liquids (Mewis et al. 2001; Simmons 1966; Simmons 1968; Tanner and Williams

1971), surfactant solutions (Khandavalli et al. 2016; Kim et al. 2013), liquid crystalline polymers (Walker et al. 2000), and colloidal suspensions and glasses (Colombo et al. 2017; Gracia-Fernández et al. 2015; Jacob et al. 2015; Jacob et al. 2019; Lin et al. 2016; Mewis and Schoukens 1978; Moghimi et al. 2019; Potanin et al. 1997; Sung et al. 2018; van der Vorst et al. 1998). While the commercial instrument makes OSP research readily available to users, the complex flow cell requires a deeper understanding of the measurement by those users. For example, despite the rectangular openings, experimental error arises from the intrinsic inhomogeneous flow field of Couette flow (i.e., shear rate varies across the gap), pumping flow due to the axial movement of the bob, and boundary forces at the leading edges of the geometry components. In order to compensate for these geometric effects, two empirical end-effect factors, the orthogonal end-effect factor and the primary end-effect factor, are implemented within the geometry constant for the instrument settings. Unfortunately, the implications of the end-effect correction are not explicitly provided in any documentation.

Understanding the correction factors due to non-idealized flow fields in this geometry is important for proper use of the instrument and obtaining accurate measurements. This is particularly important for the study of non-Newtonian fluids where the viscosity may vary by a few orders of magnitude across a narrow shear rate range. Additionally, for complex fluids, any variations in the shear strain or shear rate within the geometry could induce a structural change within the material. The current work focuses on end-effect factor calibration measurements on a commercial rotational shear rheometer using viscosity standards that range from 0.01 to 330 Pa s. The results from the study provide operational knowledge for instrument calibration and identification of the measurement window prior to collecting experimental data. These conclusions are supported by flow field information (i.e., velocity, pressure, and shear rate) during simulation of Newtonian fluids in primary or orthogonal flows, which is achieved by numerical simulations using a finite element method (FEM) software package and post-processing of simulation results.

## Methods

### Experimental

Brookfield viscosity standard silicone fluids (Ametek Brookfield, Middleboro, MA) with different viscosities of 0.0095 Pa s, 0.097 Pa s, 0.99 Pa s, 12.2 Pa s, 58.24 Pa s, 101.76 Pa s, and 331 Pa s at 25.0 °C were measured. The viscosity of the standard liquid is certified to be  $\pm 1\%$  of the reported value by the manufacturer, calibrated using NIST traceable methods. The manufacturer certified viscosity and standard deviation of silicone fluids were experimentally

verified using a 25-mm diameter 0.1 rad cone-plate geometry. The rheometer manufacturer-recommended torque and normal force calibrations were performed before the experiments, which involve hanging a precision weight from either a moment arm over a pulley or, from a hook, mounted on the transducer, measuring the torque or the normal force, and applying the new calibration factors. The experiments were performed on a strain-controlled ARES-G2 rotational shear rheometer (TA Instruments, New Castle, DE) available at NIST. There are two double-wall concentric cylinder geometries currently available for this instrument with a nominal annular gap width of either 0.5 mm or 1 mm. The schematic representation of the double-wall Couette cell is shown in Fig. 1. The bob has three rectangular openings (Fig. 1a) located at the top with centerlines spaced  $60^\circ$  apart. The inner cylinder of the cup has three rectangular openings (Fig. 1b) located at the bottom with centerlines spaced  $60^\circ$  apart. The outer cylinder of the cup can be removed from the base for the ease of cleaning. The vertical cross section of the flow cell is shown in Fig. 1c with the fluid fill level at the mid-height of the top opening of the bob. In our experiments, the fluid level is kept slightly above the top of the bob. The effects of different fluid levels on the measurements is addressed in the “Simulation” section.

A summary of the experimental techniques is provided below. The fluid was sheared by rotation of the inner and outer cylinders (cup) in the primary direction, or the axial orthogonal oscillation was applied to the center cylinder (bob).

Calibration factors are not determined when the fluid is experiencing both primary and orthogonal shear. Torque and axial force signals were measured via the force rebalance transducer through the forces exerted by the fluid on the bob. The deflection angle of the cup was measured by the optical encoder attached to the motor. The raw torque, axial force, and displacement signals were extracted from the manufacturer-supplied software. The nominal shear surface was the surface area covering the vertical distance between the top and the bottom openings. Characteristic geometrical dimensions are illustrated in Fig. 1c, i.e., the inside cup radius  $R_1$ , inside bob radius  $R_2$ , outside bob radius  $R_3$ , inside cup radius  $R_4$ , inner cylinder height  $l$ , and the immersed height or the bob effective length  $h$ . These geometry dimensions are tabulated in Table 1 and used to calculate the primary and orthogonal geometry constants. After zeroing the fixture gap (the separation between the bottom edge of the bob and the flat surface of the cup), the fixture gap or operating gap for measurement, was set to the manufacturer specified value of 8 mm, which positions the lower end of the bob at the same height with the upper rim of the bottom openings in the inner cylinder ( $l = h + 8$  mm). It is noted that the inner gap width ( $R_2 - R_1$ ) is slightly smaller than the outer gap width ( $R_4 - R_3$ ), such a design is intended to compensate for the radial changes in velocity of the moving cup walls and maintain a similar average shear rate in both gaps (Franck 2013).

Steady shear viscosity measurements (primary shear) were performed by shear rate sweeps within a typical rate range of

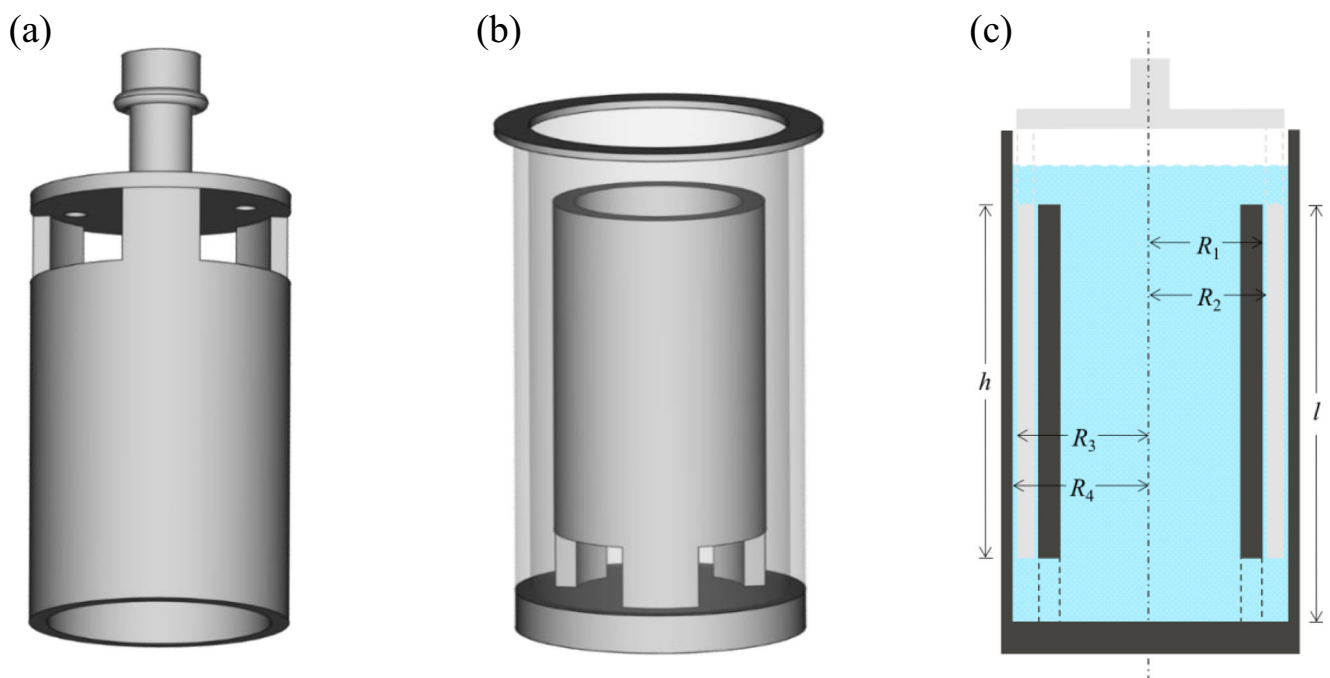


**Fig. 1** Schematics of (a) the bob, (b) the double-wall cup (the outer cylinder is shown as translucent), (c) the vertical cross section of the OSP double-wall concentric cylinder geometry, displayed for the 0.5 mm gap cell. The center cylinder (bob) is shown in gray. The outer

and inner cylinders (cup) are shown in black. The top openings on the bob and bottom openings on the inner cylinder are depicted by dashed lines. The light blue region indicates the fluid of interest within the geometry

**Table 1** Characteristic dimensions of the OSP flow cell represented in Fig. 1c and measured using a micrometer. The uncertainty is  $\pm 0.01$  mm

Parameters	Dimension (mm)	
	0.5 mm gap	1 mm gap
Inside cup radius $R_1$	13.87	13.86
Inside bob radius $R_2$	14.29	14.70
Outside bob radius $R_3$	16.50	16.04
Outside cup radius $R_4$	17.00	17.00
Inner cylinder height $l$	51.65	51.61
Immersed height $h$	43.65	43.61

approximately 0.01 to 100  $\text{s}^{-1}$ , where a lower or higher shear rate range for high or low viscosity liquids, respectively, was used based on the instrument torque sensitivity limits. The orthogonal dynamic complex viscosity (orthogonal shear) was measured by conducting orthogonal frequency sweeps from 0.1 to 40 rad/s with varying strains from approximately 0.5 to 9.4% for the 0.5 mm gap OSP cell; for the 1.0 mm gap cell, a strain amplitude range of approximately 0.5 to 5% was used due to the maximum displacement in oscillation (50  $\mu\text{m}$ ). Orthogonal amplitude sweeps were performed prior to the frequency sweeps to ensure that the applied strains were linear. Repeatability of the measurement was obtained by performing the shear rate sweeps and orthogonal frequency sweeps three times on three different loadings of each viscosity liquid. These viscosity calibration experiments were performed on two different ARES-G2 instruments at NIST using both geometries. A limited subset of fluids were investigated for the second rheometer and the 1 mm geometry to identify differences between similar instruments. All measurements were performed at 25  $^\circ\text{C}$  using the Advanced Peltier System (TA Instruments) for temperature control (standard deviation of  $\pm 0.003$   $^\circ\text{C}$ ). A temperature bath of approximately 11  $^\circ\text{C}$  was used as the thermal sink for the Peltier elements. In order to minimize thermal gradients in the transducer, the instrument was stabilized (fluid loaded and upper geometry attached) for a minimum of 30 min prior to initiating measurements.

### End-effect factors correction

Two empirical end-effect factors, the primary end-effect factor  $c_L$  and the orthogonal end-effect factor  $c_{Lo}$ , are incorporated in the geometry constants  $K_\tau$  and  $K_{\tau o}$ , which are the stress constants in the primary and orthogonal direction, that are used to compensate for the edge and boundary effects (Franck 2013). The expressions for  $K_\tau$  and  $K_{\tau o}$  are as follows:

$$K_\tau = \frac{1}{2\pi h c_L (R_2^2 + R_3^2)} \quad (1)$$

$$K_{\tau o} = \frac{c_{Lo}}{2\pi h (R_2 + R_3)} \quad (2)$$

The units for the primary stress constant  $K_\tau$  and orthogonal stress constant  $K_{\tau o}$  are  $\text{Pa N}^{-1} \text{m}^{-1}$  and  $\text{Pa N}^{-1}$ , respectively. The expressions for the strain constants are, in the primary direction,

$$K_\gamma = \frac{1}{1 - \frac{R_3^2}{R_4^2}} + \frac{1}{\frac{R_2^2}{R_1^2} - 1} \quad (3)$$

and in the orthogonal direction,

$$K_{\gamma o} = \frac{1}{R_b \ln\left(\frac{R_b}{R_a}\right)} \quad (4)$$

where  $R_b$  is the average radius of the bob, i.e.,  $R_b = \frac{1}{2}(R_2 + R_3)$ ;  $R_a$  is the difference between  $R_b$  and the average gap width, i.e.,  $R_a = R_3 - \frac{1}{2}(R_4 - R_1)$ . (Vermant et al. 1997) The strain constants for the 0.5 mm gap cell are  $K_\gamma = 33.43 \text{ rad}^{-1}$  and  $K_{\gamma o} = 2136.55 \text{ m}^{-1}$ . The strain constants for the 1 mm gap cell are  $K_\gamma = 17.24 \text{ rad}^{-1}$  and  $K_{\gamma o} = 1085.71 \text{ m}^{-1}$ .

The measurement error was determined from the repeatability study on each liquid. The propagation of error related to each end-effect factor was determined by solving Eq. 1 for  $c_L$  and Eq. 2 for  $c_{Lo}$ . The combined error for the end-effect factor was calculated according to ISO/IEC GUIDE 98–3 (2008) using the online version of the NIST Uncertainty Machine (Lafarge and Possolo 2015).

### Simulation

The simulation was performed using the computational fluid dynamics (CFD) module in the COMSOL Multiphysics version 5.4 on a Dell Precision Workstation with a 2.1 GHz dual processor CPU and 32 GB of RAM. Two incompressible Newtonian fluids with a viscosity of 1 Pa s or 100 Pa s were modeled in the double-wall concentric cylinder flow cell using an axisymmetric two-dimensional (2D) model. The laminar flow physics interface with a time-dependent study was used. The software numerically solves the model equations, i.e., the Navier-Stokes equations and the equations for conservation of mass, for velocity and pressure profiles using a FEM. The effect of varying the fluid height on the simulation results was examined. An axisymmetric 2D double-wall Couette geometry, defined in cylindrical coordinates, with an open top and an open bottom configuration (the openings depicted by the dashed lines in Fig. 1c are not present) and dimensions matching the commercial 0.5 mm gap flow cell was evaluated. A user-controlled mesh was employed, i.e., a finer mesh size is applied at the fluid-air interface; a refined mesh was added to the walls of the double gap; a finer mesh was applied at

sharp corners (corner refinement). A no-slip boundary condition was applied to the cup walls. The fluid-air interface was considered as a free surface using laminar two-phase flow with a moving mesh boundary condition. A surface tension of 63 mN/m with a zero mass flux was applied at the fluid-free surface. The moving mesh method is a convenient approach to model the free surface as a geometrical surface separating two domains as long as no topological changes are anticipated. For primary rotational shear, the swirl flow feature is used to apply the motion in the rotational direction at a nominal shear rate  $\dot{\gamma} = 1 \text{ s}^{-1}$ . For orthogonal oscillatory shear, the motion of the bob was specified by prescribing the mesh displacement to the bob boundaries under the moving mesh node with a deforming domain. The orthogonal frequency and strain for the oscillating bob are 5 rad/s and 5%, i.e.,  $\omega_{\perp} = 5 \text{ rad/s}$  and  $\gamma_{\perp} = 0.05$ , respectively. The results were solved for a total of 2 cycles at an increment of 0.01 s with the automatic remeshing option enabled. See the manufacturer supplied CFD Module User's Guide (COMSOL 2018) for detailed information on physics interface, geometry, meshing, and solver settings.

## Results and discussion

### Calibration of end-effect factors

The expression for the primary viscosity is

$$\eta_{\parallel} = \frac{\tau}{\dot{\gamma}} = \frac{K_{\tau} \cdot M}{K_{\gamma} \cdot \Omega} \quad (5)$$

where  $\tau$  is the shear stress (Pa),  $\dot{\gamma}$  is the shear rate ( $\text{s}^{-1}$ ),  $M$  is the torque (N·m), and  $\Omega$  is the rotational velocity (rad/s). According to Eq. 5, the raw data of the torque versus velocity for Newtonian fluid viscosity standards should be linear as shown in Fig. 2a. Note that an appropriate shear rate range is used for each liquid, such that the measured torque is above the manufacturer-stated minimum transducer torque, 0.1  $\mu\text{N m}$ , for steady shear. Similarly, the orthogonal end-effect factor  $c_{Lo}$  is determined by equating the orthogonal complex viscosity from the orthogonal frequency sweep experiments with the viscosity of the calibration liquids. The orthogonal complex viscosity,  $\eta_{\perp}^*$ , is described as

$$\eta_{\perp}^* = \frac{G_{\perp}^*}{\omega_{\perp}} = \frac{K_{\tau o} \cdot F_{\perp}}{K_{\gamma o} \cdot \theta_{\perp} \cdot \omega_{\perp}} \quad (6)$$

where  $G_{\perp}^*$  is the orthogonal complex shear modulus (Pa),  $\omega_{\perp}$  is the orthogonal oscillatory shear frequency (rad/s),  $F_{\perp}$  is the orthogonal oscillation force (N), and  $\theta_{\perp}$  is the orthogonal oscillation displacement (m). The raw data of orthogonal force versus the product of orthogonal displacement and frequency

( $\theta_{\perp} \cdot \omega_{\perp}$ ) are plotted in Fig. 2b for a representative orthogonal strain amplitude of 0.05 ( $\gamma_{\perp} = 0.05$ ). The frequency sweep data at other amplitudes are shown in Fig. S1 for the 12 Pa s viscosity liquid, indicating that the measurement results are invariant for all strains. The force resolution limit of the orthogonal force transducer is represented by a dashed line in Fig. 2b, and data below this line (open symbols) have values that are less than the resolution of the instrument. Data for the 0.01 Pa s viscosity standard is not measurable due to the force resolution limit of the axial normal force transducer in oscillation, 0.001 N, specified by the manufacturer.

The corrected primary viscosity and orthogonal complex viscosity are shown in Fig. 2c and Fig. 2d. The low-force limit has been translated as minimum measurable orthogonal complex viscosities, depicted by the dashed line in Fig. 2d. For either measurement, a Newtonian response, i.e., constant  $\eta(\dot{\gamma})$  or  $\eta^*(\omega)$ , is observed for each calibration liquid, and the viscosity for each standard is taken as the average value of the data across the valid shear rate or angular frequency range.

The previous discussion considers only when the viscosity of the fluid is sufficient to meet the instrument measurement resolution. It is important to verify whether the properties of the fluid, experimental parameters, and the OSP flow cell dimensions satisfy the gap loading conditions. For the investigated frequency and silicone fluid viscosities, the shear wavelength ( $\lambda_s$ ) of the mechanical oscillation in a viscous medium is calculated following Schrag (1977) and White and Schrag (1999), and the results are shown in Fig. S2a in the Supplementary information (ESM 1). The shear wavelength decreases with the increasing frequency or with decreasing viscosity. The Schrag gap loading limit is then examined in terms of the ratio, ( $\lambda_s/D$ ), of  $\lambda_s$  to the gap width ( $D$ ) for the two flow cell designs (Fig. S2b). According to Schrag (1977), the  $\lambda_s/D$  should be greater than 80 to ensure that there is no influence of the mechanical properties of the medium on the measurement results, or the gap loading condition is satisfied. In this limit, the shear wave propagates across the gap without significant damping or phase shift, such that the fluid away from the driving surface experiences the same oscillatory motion as the fluid in contact with the moving surface. A combination of low frequency oscillation, high viscosity, or small gap size is helpful to meet the Schrag gap loading limit. Those aspects have also been discussed in Ewoldt et al. (2015), where a general guideline to identify an operating window is provided. As seen in Fig. S2b, the higher frequency data for the 0.1 Pa s liquid and the 0.01 Pa s liquid are less than this limit for both the 0.5 mm and 1.0 mm gap geometries. Therefore, although these higher frequency data for the 0.1 Pa s silicone are greater than the instrument force resolution (as shown by the black solid triangles in Fig. 2b), they are not reliable based on the Schrag gap loading limit analysis. For the 1.0 mm gap cell, the  $\lambda_s/D$  ratio is half of the value for

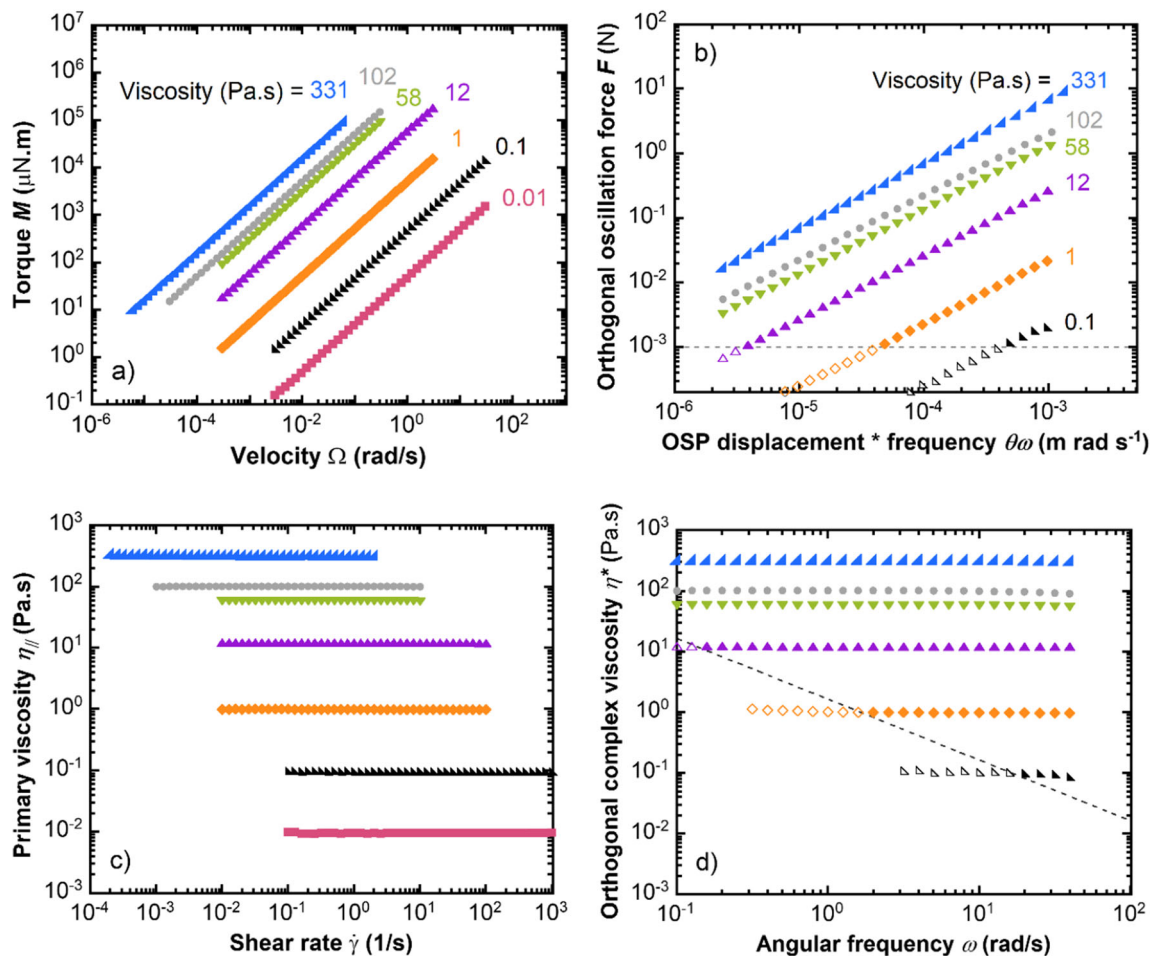


**Fig. 2** Raw data for viscosity calibration measurements in rotational (a) and orthogonal (b) directions measured at 25 °C. Corrected steady shear viscosity as a function of shear rate in the rotational direction (c) and corrected orthogonal complex viscosity as a function of frequency in the orthogonal direction (d). The data shown in (b) and (d) are frequency sweeps at a representative orthogonal strain of 0.05 ( $\gamma_L = 0.05$ ). The minimum axial force resolution in oscillation for the instrument is shown by the dashed line in (b). The dashed line in (d)

represents the limit of minimum measurable complex viscosity. Open symbols represent those below the instrument resolution. Standard uncertainties of  $\pm 0.001 \mu\text{N m}$  for the torque in (a) and 0.001 N for oscillation force in (b) are assumed based on manufacturer specifications. The standard uncertainty for the viscosity in (c) is within 0.6% of the measurement, and for complex viscosity in (d) is within 0.1%. Different colors and symbols represent measurements performed on different viscosity standards. View in color for best clarity

the 0.5 mm cell, which shifts the gap loading limit to lower frequencies. Therefore, the applicable frequency range is more limited for low viscosity materials using the wider gap cell. A detailed analysis of linear viscoelastic wave propagation is provided in Schrag's original paper (Schrag 1977), in which the expressions for correcting the measured modulus and phase angle is presented as a function of fluid properties and positions in the gap. The data outside of the gap loading limit range may still be used if the corrections are applied for a strain-controlled rheometer with a separate motor transducer (Läuger and Stettin 2016).

The primary end factor  $c_L$ , solved by combining Eqs. 1 and 5, is plotted versus viscosity in Fig. 3a. The results of  $c_{L0}$  solved by combining Eqs. 2 and 6 are shown in Fig. 3b. Both factors are obtained by performing measurements in either the primary or orthogonal direction independently (i.e., in

the absence of the flow in the other direction). The  $c_L$  is found to vary from 1.16 to 1.21 over more than four decades of viscosity (Fig. 3a) in this work. In other words, without correction, the measured value of the viscosity is 16 to 21% higher than the true value. There was no significant difference in  $c_L$  between the two gap geometries investigated in this work. The standard deviation from the repeatability study for each liquid in Fig. 3a, represented by the error bars, is small. The  $c_L$  appears to vary from a high value to a lower value with increasing fluid viscosity. However, the combined error for  $c_L$ , obtained using the NIST Uncertainty Machine (see "Experimental" section), is approximately 2.4% of the mean. This range is shown by the dotted lines in Fig. 3a, which bounds  $c_L$  across 5 orders of magnitude in viscosity, indicating that this seemingly oscillatory trend across the filled blue circles for  $c_L$  is related to a systematic error.

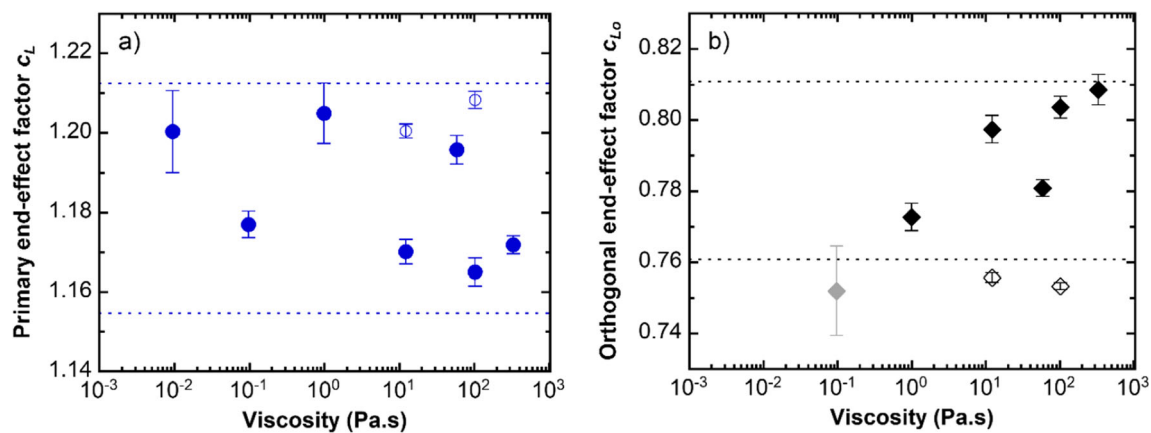


**Fig. 3** (a) The primary end factor  $c_L$  and (b) the orthogonal end factor  $c_{Lo}$  as a function of viscosity. The error bar represents standard deviation from three repeat runs on at least three different specimens. The filled and open symbols represent data obtained using the 0.5 mm double gap OSP cell and 1.0 mm double gap OSP cell, respectively, on the primary rheometer.

The correction is anticipated for Couette type viscometers due to the non-uniform shear rate distribution over the annular cross section of the geometry. For example, a Couette with the bob as the stator and the cup as the rotor, the shear rate  $\dot{\gamma}$  decreases from the bob wall to the cup wall. The working equations relating the shear rate to angular velocity are often derived with approximate methods or infinite series solutions (Krieger 1968; Krieger and Elrod 1953; Yang and Krieger 1978). Therefore, implicit assumptions such as a narrow gap between the cylinders and infinitely long cylinders are often made to achieve an analytical solution for the shear rate, such that any torque exerted on the bob end faces as well as any disturbance to the flow in the annular gap because of the proximity of the ends, which are referred to as “end effects,” are neglected. For commercial Couette viscometers, the error induced by the end effects are conventionally absorbed in the instrument constant by an end-effect correction factor (Highgate and Whorlow 1969; Kobayashi et al. 1991; Lindsley and Fischer 1947). For a standard conical bottom concentric cylinder viscometer,  $c_L = 1.10$  for Newtonian liquids (International Organization for Standardization 1993). It is noted that the implemented corrections are valid only for the calibration liquids, which are normally performed with a Newtonian fluid; hence, the correction factor must be determined experimentally for each type of measuring system geometry. For the double gap system, similar inherent issues occur with the non-uniform shear rate in the concentric annulus and additional torque acting on the bob end surfaces. Any small misalignment of the bob with respect to the coaxial double-walled cup may also induce distortion in the flow field that leads to additional error. The finite length effect, or “end effect,” is associated with both the upper and bottom ends of the bob that contribute to the measured torque. Note that the standard operating procedure for the commercial OSP geometry does not require the flow cell to be filled exactly level to

Note in (b) that  $\eta = 0.01$  Pa s is below the instrument normal force resolution (not shown), thus outside the measurement window and  $\eta = 0.1$  Pa s (gray diamond) is outside the gap loading conditions (see text for details). The dotted lines in each figure represent the combined error of the mean of the end-effect factor for each viscosity liquid

the upper rim of the inner cylinder, such that the end effect associated with the top region is not negligible. In a real experiment, other sources of error also become a factor, including wall slip, secondary flows, eccentricities, and viscous heating (Macosko 1994). The 16 to 21% error observed for Newtonian fluids signifies the importance of performing calibrations for the system, as the correction needed is much greater than the default  $c_L$  value (1.065) provided by the manufacturer that presumes 6.5% error correction.

The intent of the OSP cell is to probe structure non-destructively in complex fluids orthogonal to the primary shear flow. Orthogonal end-effect can play a significant role in the ability to accurately quantify this perturbation. The orthogonal end-effect factor,  $c_{Lo}$ , ranges from 0.75 to 0.81 for viscosities from 1 to 331 Pa s (Fig. 3b), meaning that the orthogonal measurement overestimates the viscosity by 19 to 25% without correction. The standard deviation from the repeatability study for each liquid, represented by the error bars in Fig. 3b, is also small. This correction is expected due to the limited amount of pumping effect generated by the bob motion displacing fluid, which is alleviated by the openings on the inner cylinder so that the flow can evacuate into the inner cylinder reservoir; however, this effect is not completely eliminated. The comparison between an open and a closed bottom cell configuration has been investigated by Colombo et al. (2017), where they report an approximately 10% overestimation of the viscosity for the open bottom geometry; for the closed bottom configuration, the offset was as high as 2 orders of magnitude compared with the actual value due to pressure-driven Poiseuille flow in the annular gap. While the presence of openings and a large central fluid reservoir in the commercial flow cell reduce the pumping effect, a non-zero correction factor is not surprising. The filled diamonds in Fig. 3b represent  $c_{Lo}$  for the 0.5 mm gap cell, which required less correction than the 1.0 mm gap cell (open diamonds). One

might be tempted to apply a linear fit to the  $c_{Lo}$  data for the 0.5 mm gap cell (filled black diamonds in Fig. 3b). However, this is misleading since no dependence of the errors on the Newtonian fluid viscosity is expected in the gap-loading limit as the shear stresses and pressure gradients are proportional to the viscosity in the Navier-Stokes equation (Zeegers et al. 1995). Note that the data point at  $\eta = 0.1$  Pa s (gray diamond) is out of the gap loading limit range, as discussed earlier (see Fig. S2b), and therefore outside the measurement range for these geometries. The combined error for  $c_{Lo}$  is approximately 3.1%. This range is shown by the dotted lines in Fig. 3b, which bounds  $c_{Lo}$  across 3 orders of magnitude in viscosity. With this understanding,  $c_{Lo}$  does not vary with fluid viscosity and any observed trends are within the systematic error. As with the primary shear correction factor, users should establish these end-effect correction values on their systems with Newtonian fluids spanning the viscosity range of the fluid of interest.

We performed the same calibration experiments using two viscosity standards and both flow cell geometries on a second ARES-G2 instrument located at NIST. The two liquids of choice, i.e., 12.2 Pa s and 101.76 Pa s, satisfy the gap loading condition and meet the minimum signal-to-noise ratio in the torque and normal force signals. They also represent viscosity ranges reported for many colloidal gels or soft materials. The end-effect factor results are shown in Fig. S3. For the primary shear, the primary end-effect factors from the second instrument (rheometer 2) appear to be in a comparable range with those observed for the primary instrument (rheometer 1). For the orthogonal end-effect factors, the values for the second rheometer are less than those of the primary instrument, indicating a larger offset or correction factor is required to shift the complex viscosity. This finding suggests the importance of performing calibration for each instrument and flow cell geometry. At this time, there is no clear source for the difference between the instruments, although it is likely due to inherent differences in the transducer transfer functions, the mismatch of the alignment between bob and cup walls, or sensitivity to the systematic error. For completeness, the transducer transfer function parameters were directly exported from the manufacturer-supplied software and tabulated in Table S1. The 19 to 25% error observed for Newtonian fluids signifies the importance of performing calibrations for the system, as the orthogonal end-effect correction needed is much greater than the default  $c_{Lo}$  value (0.857) provided by the manufacturer that presumes 14.3% error correction.

## Velocity and pressure profiles

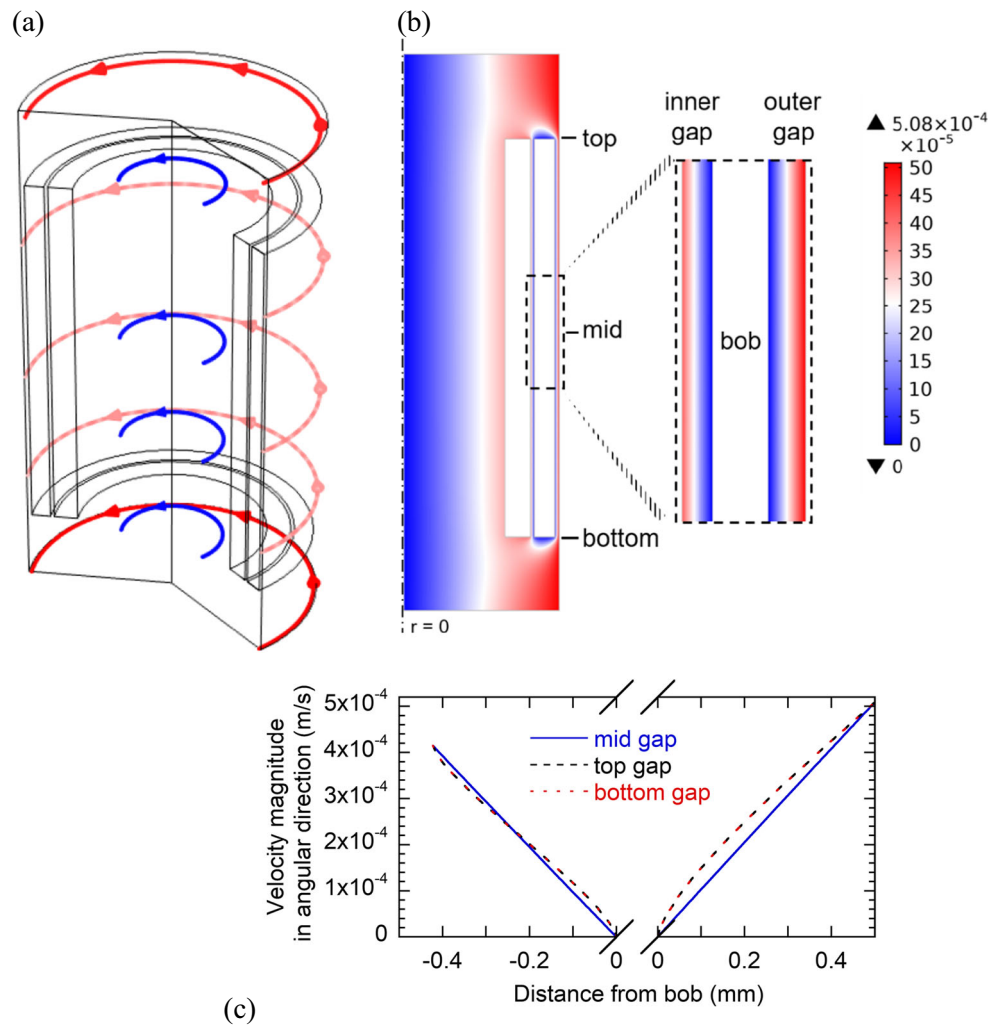
To better understand the origins and quantify various contributions to the end effects in the double-wall concentric cylinder geometry, numerical simulations were performed. An axisymmetric 2D model with appropriate boundary conditions is

investigated, which is a close approximation and convenient simplification to the three-dimensional problem. The flow patterns during primary and orthogonal shear operations are visualized by surface plots and contour plots of the velocity and pressure fields. Additionally, the end-effect factors are estimated from the numerical solutions to quantify different sources and magnitudes of error in a straightforward manner. A detailed examination on complicated flow properties such as flow instabilities (secondary flow regimes, recirculation zones, etc.) and bifurcation are beyond the scope of the present work.

The velocity fields for the 1 Pa s Newtonian fluid in the double-wall concentric cylinder geometry with a fluid level equal to the maximum height of the upper opening and undergoing only primary rotation are shown in Fig. 4a. The results are shown for a fully developed steady state velocity profile. The cup consists of the inner and outer cylinders (representing the cup) rotating at a constant angular velocity while the center cylinder (representing the bob) is stationary. This motion creates a linear shear deformation profile in the double gap, as shown in Fig. 4b, in which the velocity magnitude is highest at the outer surface of the inner rotating cylinder and the inner surface of the outer rotating cylinder. As shown in Fig. 4c, where the angular component of the velocity field is plotted as a function of the distance from the bob wall, the velocity gradient is nearly linear throughout the inner and outer gaps. A slight deviation from a linear profile is predicted in the vicinity of the top and bottom bob ends, as shown by the black dashed line and red dotted line, respectively. The shear rate distribution in the annular gap at the mid-height of the bob is shown in Fig. S4a. As expected, a non-uniform shear rate is observed in the concentric annulus, i.e., the shear gradient decreases radially outwards.

As discussed in the experimental measurements, the orthogonal oscillation represents a more complicated interaction between the moving surfaces and the fluid. The velocity fields for the orthogonal oscillation, oscillating bob moving downward with a velocity of  $1.17 \times 10^{-4}$  m/s, is shown in Fig. 5. The velocity field during a two-cycle oscillation is shown in Movie S1 for a revolution 2D view. Conservation of mass is checked by calculating the mass flux error across the air-fluid boundary, which is defined as the mass flux across the boundary (approximately  $10^{-7}$  kg/s) normalized by the mass flux within the fluid domain. This yields a relative mass error of approximately  $10^{-4}$ , indicating a sufficiently low error. As illustrated by the streamlines in Fig. 5a, the fluid adjacent to the bob is moving downward which generates a flow field that propagates into the center of the inner cylinder. This propagating flow field also induces a flow field at the center of the inner cylinder reservoir. The velocity of this field is greater than that of the moving bob and circulates back into the annulus at the fluid-air interface, which is a consequence of the cylindrical geometry for an equivalent volumetric flow rate

**Fig. 4** Simulation results of primary steady shear at a nominal shear rate of  $1 \text{ s}^{-1}$  for a  $1 \text{ Pa s}$  Newtonian fluid in the double-wall concentric cylinder geometry with open top and open bottom configuration. **(a)** Streamline plot of the velocity field for the 2D revolution results. The streamline color represents velocity magnitude (m/s) corresponding to the color scale in **(b)**. **(b)** Surface plot of the velocity magnitude (m/s) for the 2D axisymmetric model. The entire bob view is shown on the left and an enlarged view of the fluid in the black dashed box is shown on the right. The maximum and minimum values are indicated along with the vertical color bar. **(c)** Velocity profile in the angular direction across the double gap at three different height levels, i.e., the top end, mid-height, and the bottom end of the bob. The zero position is at the surface of the bob wall, where the inner gap is indicated by negative distance, and the outer gap is indicated by positive distance. View in color for best clarity



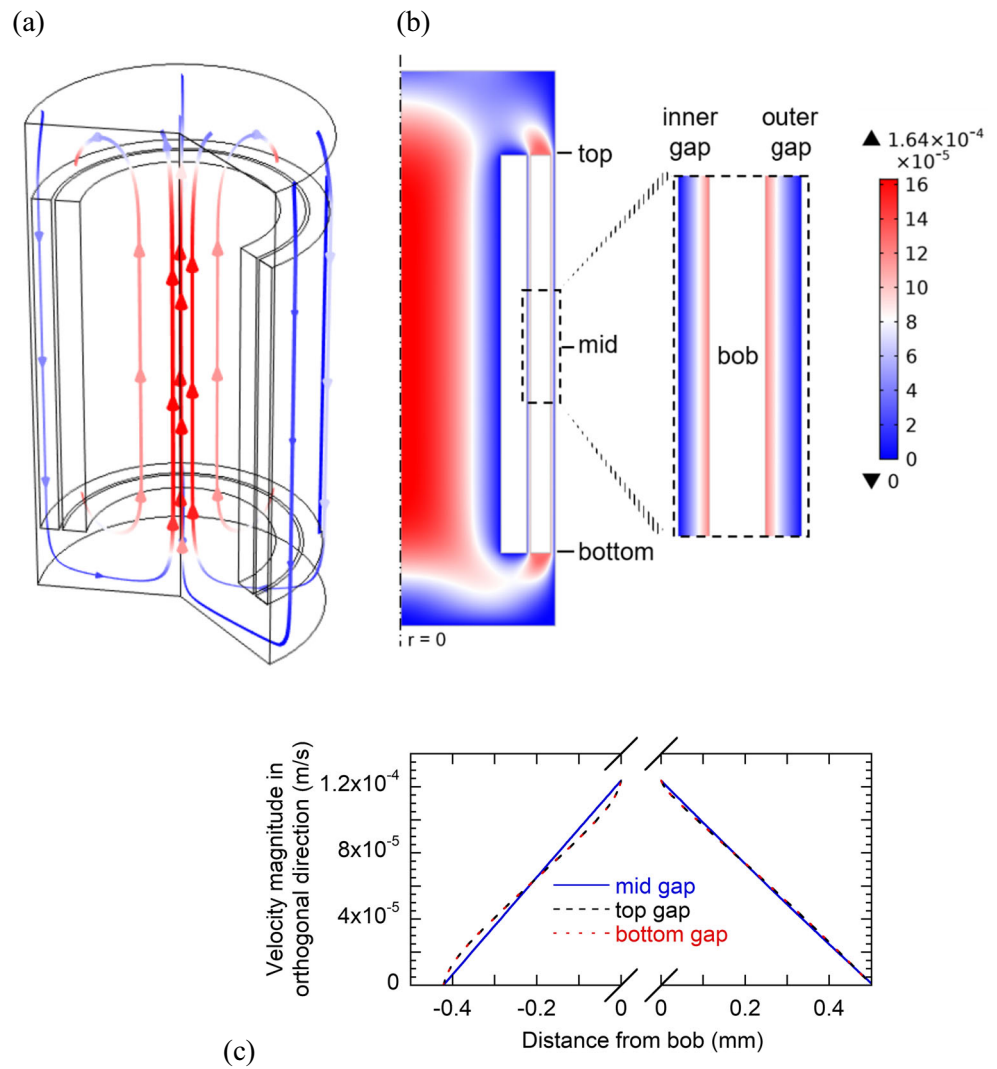
along the radial direction. The shear deformation, driven by the drag flow between the moving bob surface and fixed double-wall cup, is generally linear across the double gap as shown in Fig. 5b, where the maximum velocity occurs at the bob walls. Similar to the primary shear direction simulation results, the velocity gradient is shown in Fig. 5c for the top, mid, and bottom locations along the bob. The bob ends result in positive and negative deviations, shown by the dashed and dotted lines, from the linear profile at the mid-height. The bob end effect is greater for the smaller inner gap. The shear rate in the cross section at the mid bob height is shown in Fig. S4b, where a higher shear rate in the inner gap (an average of  $0.29 \text{ s}^{-1}$ ) is observed as compared with that in the outer gap (an average of  $0.24 \text{ s}^{-1}$ ). The average shear rate across both gaps is  $0.27 \text{ s}^{-1}$ , which overestimates the theoretical value,  $0.25 \text{ s}^{-1}$  ( $\omega_{\perp} = 5 \text{ rad/s}$  and  $\gamma_{\perp} = 0.05$ ), by approximately 8%.

While the focus to this point has been on the fluid at the moving boundaries or the transition into the fluid reservoir, it is important to realize that the cup is a finite size. A secondary benefit of the simulation is the ability to visualize how flow

fields interact with both the bottom walls of the cup and the free air interface. The impingement of streamlines with these interfaces has the potential to affect the flow field as the fluid enters and exits the annulus. Figure 6 shows an enlarged view of the velocity profiles for the top and bottom of the OSP geometry. Due to the axial motion of the bob, there is clearly a distortion in the flow field as shown by the red regions above the bob top end (Fig. 6a) as well as below the bob bottom end (Fig. 6b), although the open top and open bottom configurations offer a passage to the inner reservoir.

The velocity profiles help to illustrate the movement of the fluid during the oscillatory measurement, but the velocity gradients lead to a pressure gradient that is responsible for residual pumping from the annulus to the reservoir. Figure 7 shows the pressure fields in the geometry at the same downward velocity for the bob. Due to the displacement of the fluid by the axial oscillation of the bob, a Poiseuille-like pressure drop in the annular gap is observed, i.e., the pressure gradient is uniformly distributed along the axial direction without any radial changes. The pressure drop is nearly linear as shown

**Fig. 5** Simulation results of orthogonal oscillatory shear at  $\omega_{\perp} = 5$  rad/s and  $\gamma_{\perp} = 0.05$  for a 1 Pa s Newtonian fluid in the double-wall concentric cylinder geometry with open top and open bottom configuration. **(a)** Streamline plot of the velocity field for the revolution 2D results. The streamline color represents velocity magnitude (m/s) corresponding to the color scale in **(b)**. **(b)** Surface plot of the velocity magnitude (m/s) for the 2D axisymmetric model. The entire bob view is shown on the left and an enlarged view of the fluid in the black dashed box is shown on the right. The maximum and minimum values are indicated along with the vertical color bar. Results are shown for the oscillating bob moving downward at a velocity of  $1.17 \times 10^{-4}$  m/s. **(c)** Velocity profile in the orthogonal direction over the double gap at three different height levels, i.e., the top end, mid height, and the bottom end of the bob. The zero position is at the surface of the bob wall, where the inner gap is indicated by negative distance, and the outer gap is indicated by positive distance. View in color for best clarity



in Fig. S5, and the pressure differences in the inner and outer gap are 0.49 Pa and 1.26 Pa, respectively. The pressure fields above the bob top end and below the bob bottom end show

drastic variations. As shown in Fig. 7, the peak pressure and maximum pressure gradient appear near the edges of the bob ends, as indicated by the dense contour lines in those regions.

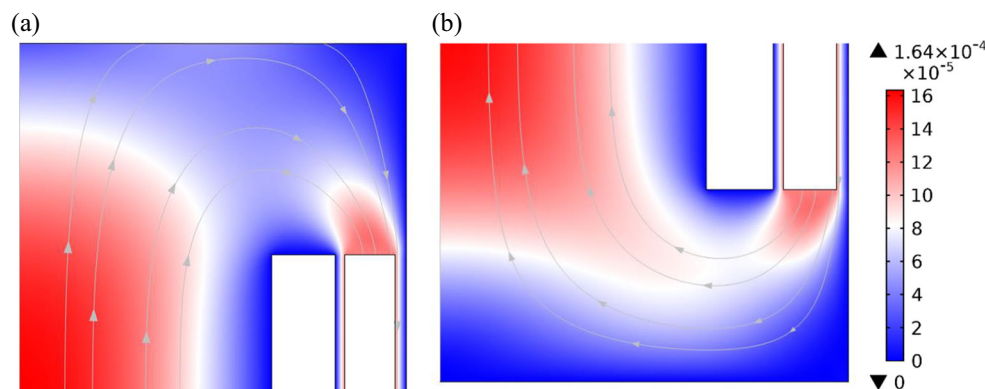


**Fig. 6** Surface plots of the velocity magnitude (m/s) for the 2D axisymmetric model with open top and open bottom configuration for top **(a)** and bottom **(b)** view. Results are shown for the oscillating bob

moving downward at a velocity of  $1.17 \times 10^{-4}$  m/s. The maximum and minimum values are indicated along with the vertical color bar. The streamlines represent velocity field. View in color for best clarity

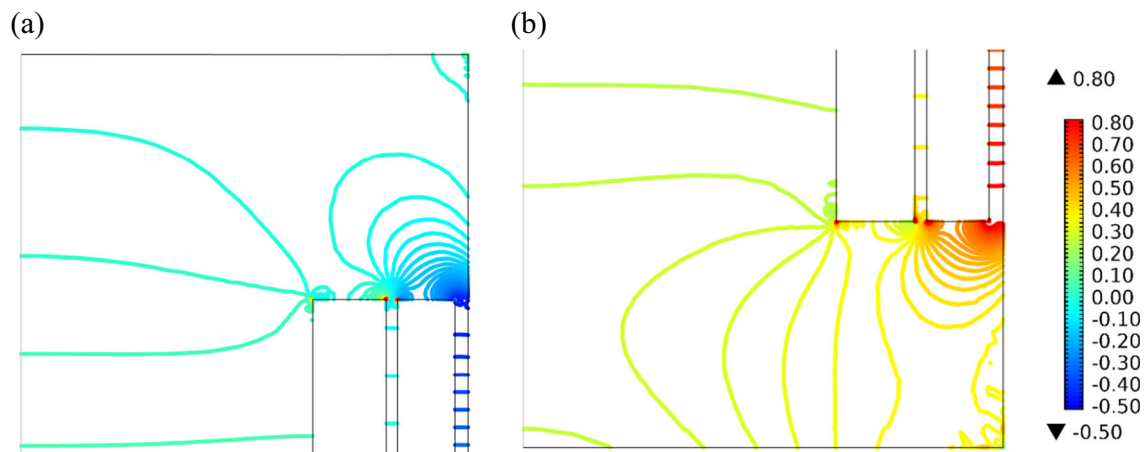


**Fig. 7** Pressure contours (Pa) for the 2D axisymmetric model with open top and open bottom configuration for top (a) and bottom (b) view. Results are shown for the oscillating bob moving downward at a

velocity of  $1.17 \times 10^{-4}$  m/s. The maximum and minimum values are indicated along with the vertical color bar. View in color for best clarity

This observation recalls that avoiding sharp corners in the geometry design is beneficial to avoid undesirable complex flows in general (Moffatt 1964), as well as to prevent cavitation (Tanner and Williams 1971). Figure 7b suggests that the bob end pressure field could be affected by the distance to the cup bottom. Linsley and Fischer (1947) have previously shown that the end-effect is dependent on the separation between the bottom of bob and cup for a Couette-type viscometer. Since the pressure exerted on the bob end surfaces is parallel to the viscous drag force in the orthogonal direction, the additional force contributed by the pressure gradient is an important aspect of the flow field when estimating the total orthogonal force on the bob during oscillation.

### Error estimation from simulation

The velocity and pressure fields provide a visualization of the non-idealities in the fluid motion within the double-wall concentric cylinder geometry. Of interest here is to utilize those specific end effects captured by simulation to estimate the end-effect errors and compare those with our calibration experiments. For the primary rotational shear, the total force is calculated by integrating the local shear stress, i.e., the viscous stresses in the radial direction at the bob walls, over the bob surface area. This gives a viscosity of 1.03 Pa s (Eq. 5), which overestimates the theoretical viscosity by 3%. The main source of error arises from the additional torque exerted on the end (top and bottom) surfaces of the bob during the primary shear.

For the orthogonal oscillatory shear, the total oscillation force ( $F_{\perp}$  in Eq. 6) consists of the viscous force exerted on the bob side walls (inner and outer cylindrical surfaces) and the pressure force acting on the bob ends (top and bottom end surfaces). The viscous force and pressure are summed to obtain the total force on the bob, which is divided by the nominal shear area to convert to total stress on the bob. We, then

estimate the viscosity and obtain the orthogonal end-effect correction factors from Eq. 6. The results are summarized in Table 2 for different fluid levels, i.e., when the fluid level is even with the upper rim of the inner cylinder; the fluid level is at a quarter of the opening height above the bottom edge of bob opening; the fluid level is level with the upper edge of the bob opening. Errors for the three cases are 7%, 17%, and 17%, respectively, with larger errors found for the latter two fluid levels. As mentioned earlier, when the fluid level is above the upper rim of the inner cylinder, the contribution of pressure acting on the top end of the bob causes additional error. In addition to the pressure effect that contributes to approximately 9% of the total error, the viscous force is overestimated by 8% compared with the theoretical value, as a result of the increased shear rate in the double gap (Fig. S4). The simplified model (axisymmetric 2D) represented in our simulation provides an error estimation that is comparable with the error measured in the orthogonal calibration (19 to 25%).

For the case where the fluid height equals the upper rim of the inner cylinder, the viscous force is overestimated by approximately 1%, whereas the pressure contribution from the bob bottom end is reduced to 7%. This suggests that having the fluid level at exactly the same height as the upper rim of the inner cylinder is advantageous to improve accuracy. The effect of overfilling on the viscosity was studied experimentally using the 1 Pa s oil. The geometry was first filled to achieve a fluid level slightly above the upper bob end. A known volume of oil was added by micropipette to increase the fluid height above the upper rim of the bob ( $l < fh < l + d$ ). The viscosity results for different fluid levels were within experimental error (results are not shown for brevity). However, visual inspection of the fluid level while filling the cell and an accurate control of fluid volume for high viscosity liquids may be difficult to achieve in practice, we therefore recommend a consistent volume of fluid, such that fluid level

**Table 2** CFD simulation results of the viscous force, pressure, total force, and the calculated viscosity for different fluid height levels<sup>1</sup>

Fluid height level	$fh = l$	$fh = l + \frac{1}{4}d$	$fh = l + d$	Theoretical value
Viscous force (mN)	2.13	2.29	2.28	2.11
Pressure (mN)	0.13	0.19	0.20	
Total force (mN)	2.26	2.48	2.48	2.11
Viscosity (Pa s)	1.07	1.17	1.17	1
Orthogonal end factor $c_{Lo}$	0.93	0.83	0.83	1

<sup>1</sup> The simulation for the case of the fluid height equals the inner cylinder height ( $fh = l$ ), wall velocity is prescribed for the oscillation motion of the bob, whereas for the cases where the fluid height is above the upper rim of the inner cylinder ( $fh = l + \frac{1}{4}d$  and  $fh = l + d$ , where  $d$  is the height of the upper opening), the mesh displacement condition is applied to the bob walls for the oscillation motion. In all cases, the bob oscillates with an orthogonal frequency of 5 rad/s and an orthogonal strain of 5%, i.e.,  $\omega_{\perp} = 5$  rad/s and  $\gamma_{\perp} = 0.05$

is slightly above the upper opening edges on the bob to maintain a fixed bob effective length (thus a fixed nominal shear surface) while minimizing the error associated with the top end of the bob. The fluid level can be roughly checked by the wetted fluid contact line on the top of the bob by lifting it slightly out of the reservoir. When lowering the bob into the fluid, care must be taken to avoid cavitation or transducer overload, especially for highly viscous fluids or fluids exhibiting a yield stress. The filling process may require long wait times to achieve proper fluid level given the small gap size and complex cell design.

The simulation results for a 100 Pa s Newtonian fluid are similar and yield an approximately 17% offset for the fluid height greater than the bob height. As long as the measurement operates in the gap loading limit, Stokes flow (or creeping flow) is anticipated, in which the shear stresses and pressure gradients are proportional to the viscosity, such that there should be no dependence of viscosity on experimental error (Zeegers et al. 1995). This is consistent with the observation that no systematic trend of the end factors on the viscosity is found from our viscosity calibration experiments (Fig. 3). Note that for the 0.1 Pa s liquid, whose orthogonal end factor is lower than the other liquids, the gap loading limit did not hold for the high frequency measurements.

The simulations provide insights into possible improvements for the geometry design. A straightforward strategy is either to decrease the pressure contribution or to increase the viscous contribution, such that the total oscillation force is dominated by the viscous part. Therefore, it is desired to have the bob end surfaces as small as possible, or to have the active shearing surface (inner and outer bob cylindrical surfaces) as large as possible. For the former, an effective approach is to reduce the bob thickness. For the latter, given the physical constraints of the Advanced Peltier System (APS) that limits the overall diameter and height of the geometry, the only way to achieve a greater shear surface area is to increase the bob effective length. This can be achieved by reducing the height of the upper openings on the bob and extending the height of the inner cup wall. It is noted that the upper bob openings are designed to minimize surface tension effects

(Franck 2013). If the upper openings were completely removed to maximize shear surface area, the surface tension contribution resulting from the increase in fluid-air-bob interfacial area would require an additional correction factor, especially for low frequency data. This effect is purely elastic and fluid-dependent. The correction can be applied to the raw data through the elastic coefficient of the transducer (Vermant et al. 1997). For a commercial rheometer with a constant elastic coefficient ( $K$  in Table S1) embedded in the final transducer design, the upper bob opening configuration serves as a remedy for this issue. (Franck 2013) With all that said, this paper aims to provide operational knowledge for general users of the commercial OSP rheometer, further details on advanced correction procedures for a custom-manufactured geometry, or for experienced users with access to the transducer parameters, is beyond the scope of this work, but worth mentioning here for completeness.

The present calibration procedures and end-effect correction factors are only valid for Newtonian fluids. For non-Newtonian liquids, the end correction may be considerably larger, depending on the rheological characteristics of the fluid and the shear rate range of interest (Highgate and Whorlow 1969). For a viscoplastic fluid with a yield stress, the material would behave as a solid with slip layers confined at the walls when sheared in the pre-yield regime (Princen 1985). Besides wall slip, other detrimental effects for non-Newtonian liquids such as sample fracture and normal stress effects may also increase the severity of measurement error (Macosko 1994).

## Conclusions

In this work, viscosity calibration measurements were carried out on a commercial rotational shear rheometer equipped with a double-wall concentric cylinder geometry. The primary shear and orthogonal shear end-effect factors were determined using a range of standard Newtonian fluids from 0.01 to 331 Pa s. Two different gap size geometries were investigated on two strain-controlled rheometers. Detailed information on the calibration procedures and end-effect factor determination methods are

provided. The corrections needed for the primary steady shear viscosity are approximately 16 to 21%; whereas for the orthogonal complex viscosity, the errors are approximately 19 to 25%. These values are higher than those provided by the manufacturer, and the variations in the end-effect factors on different viscosities are bounded by the estimated combined error. A further understanding of the end correction and flow field is accomplished by computational fluid dynamics simulation. We show that an approximately linear shear deformation profile for the fluid, in the double gap, are attained in both primary steady shear and orthogonal oscillatory shear deformations. A detailed picture of the velocity and pressure distributions for fluid above the bob top end and below the bob bottom end show distortions in the flow field due to the residual pumping effect from the axial oscillation motion of the bob. Through careful analysis of the viscous force, pressure, and total force over the bob surface, the overestimation of the orthogonal viscosity is attributed to the pressure forces exerted on the bob end surfaces (9%) and an increased shear rate in the double gap that result in higher viscous stresses on the bob cylindrical surfaces (8%). For the steady shear measurements in the primary direction, a large error (16 to 21%) is observed, whereas the simulation predicts a lower error (3%). The errors in the primary viscosity may arise from a range of sources, but one prominent reason may be due to the non-homogeneous shear field in this complicated geometry. Furthermore, the installation of the flow cell requires precise alignment of the axes of the cup and bob and positioning of the bob at the correct gap height; any slight deviations potentially introduce additional experimental uncertainties. Therefore, a good practice is to use this complicated geometry only when there is a need to operate in the orthogonal mode.

From the simulation results on the effect of different fluid height, it is advisable to fill the geometry in such a way that the fluid is level with the upper rim of the inner cylinder, which helps reduce the error associated with the top end of the bob. However, orthogonal complex viscosity measurements were insensitive to the fluid level above the top end of the bob. Since visual inspection of the fluid level is not practical and precise volumetric filling for high viscosity liquids is difficult, a consistent volume of fluid that achieves a fluid level slightly above the upper rim of the inner cylinder is recommended for this commercial geometry. In this way, a fixed bob effective length or nominal shear surface is maintained, while the end-effect associated with the bob top end is minimized.

It is highly recommended to use Newtonian fluids with known viscosities representative of the application range to calibrate each instrument prior to any measurements; significant errors in the measured viscosities or complex shear moduli in the range of 16% or more may occur otherwise. The end-effect factors obtained from a second instrument in this work fall into a different range for the orthogonal measurements, but the errors are similarly appreciable. It is important for the users to keep in mind that the actual corrections needed vary

among instruments and could be material-dependent (e.g., non-Newtonian fluids), and these are not necessarily addressed in the “embedded” geometry constants. The present calibration procedures and end-effect issues are for Newtonian fluids, but suggest that carrying out orthogonal superposition measurements using the current test setup with non-Newtonian and viscoelastic fluids may well be problematic as the calibration problems for such fluids could be more severe. The fluid field information for Newtonian fluids from this work provide a benchmark for future simulations using non-Newtonian fluids. Additionally, the operational knowledge (i.e., consistent filling) and measurement window (i.e., viscosity and frequency) outlined in this work are beneficial in view of the growing interest of applying this technique for the investigation of other structured fluids.

**Acknowledgments** The authors thank Prof. Jan Vermant (ETH Zurich), Dr. Paul Salipante (NIST), and Dr. Fred Phelan (NIST) for their insights and expertise that greatly assisted this research. We also thank Dr. Siva Tholeti (COMSOL, Inc.) for the advices on simulation and the communications with TA Instruments Rheology team that sparked our initial interest in this research. Dr. Ryan Murphy and Dr. Paul Butler (NIST) are acknowledged for the assistance with the access of the rheometer and OSP geometry at NIST NCNR. We thank Dr. Paul Salipante (NIST) for the careful review of an early draft.

#### Greek letters

$\omega_{\perp}$  bob orthogonal oscillatory shear frequency (rad/s)  
 $\gamma_{\perp}$  bob orthogonal oscillatory shear strain amplitude  
 $\tau$  shear stress (Pa)  
 $\dot{\gamma}$  shear rate ( $\text{s}^{-1}$ )  
 $\Omega$  cup angular velocity (rad/s)  
 $\eta_{\parallel}$  primary steady shear viscosity (Pa s)  
 $\eta_{\perp}^*$  orthogonal complex viscosity (Pa s)  
 $\theta_{\perp}$  orthogonal oscillation displacement (m)  
 $\lambda_s$  shear wavelength (m)

**Funding information** Funding from the National Institute of Standards and Technology (Award # 70NANB15H112) is gratefully acknowledged.

#### Compliance with ethical standards

**Conflict of interest** The authors declare that they have no conflict of interest.

**Disclaimer** Certain commercial equipment, instruments, or materials are identified in this paper in order to specify the experimental procedure adequately. Such identification is not intended to imply recommendation or endorsement by the National Institute of Standards and Technology, nor is it intended to imply that the materials or equipment identified are necessarily the best available for the purpose. This paper is an official contribution of the National Institute of Standards and Technology, US Department of Commerce; not subject to copyright in the USA.

**Nomenclature**  $R_1$ , inside cup radius (m);  $R_2$ , inside bob radius (m);  $R_3$ , outside bob radius (m);  $R_4$ , outside cup radius (m);  $R_b$ , average radius of the bob (m);  $R_g$ , difference between  $R_b$  and the average gap width (m), defined in Eq. 4;  $l$ , inner cylinder height (m);  $h$ , bob effective length (m);  $c_L$ , primary end-effect factor;  $c_{L\perp}$ , orthogonal end-effect factor;  $K_{\parallel}$ , primary stress constant ( $\text{Pa N}^{-1} \text{m}^{-1}$ );  $K_{\perp}$ , orthogonal stress constant ( $\text{Pa N}^{-1}$ );

$K_{\gamma}$ , primary strain constant ( $\text{rad}^{-1}$ );  $K_{\gamma o}$ , orthogonal strain constant ( $\text{m}^{-1}$ );  $M$ , torque (N m);  $F_{\perp}$ , orthogonal oscillation force (N);  $G_{\perp}^*$ , orthogonal complex shear modulus (Pa);  $h$ , fluid height (m);  $d$ , upper opening height (m);  $D$ , gap width (m)

## References

- Birnboim MH, Ferry JD (1961) Method for measuring dynamic mechanical properties of viscoelastic liquids and gels; the gelation of polyvinyl chloride. *J Appl Phys* 32:2305–2313
- Colombo G, Kim S, Schweizer T, Schroyen B, Clasen C, Mewis J, Vermant J (2017) Superposition rheology and anisotropy in rheological properties of sheared colloidal gels. *J Rheol* 61:1035–1048
- COMSOL AB (2018) *CFD Modules User's Guide*, COMSOL Multiphysics™ v. 5.4. COMSOL AB, Stockholm, Sweden
- Ewoldt RH, Johnston MT, Caretta LM (2015) Experimental challenges of shear rheology: how to avoid bad data. In: Spagnolie S. (eds) *Complex Fluids in Biological Systems*. Biological and Medical Physics, Biomedical Engineering. Springer, New York, NY, pp 207–241
- Franck A (2013) Orthogonal superposition on the ARES-G2. TA instruments, application note, APN035
- Gracia-Fernández C, Gómez-Barreiro S, Elmoumni A, Álvarez A, López-Beceiro J, Artiaga R (2015) Simultaneous application of electro and orthogonal superposition rheology on a starch/silicone oil suspension. *J Rheol* 60:121–127
- Highgate DJ, Whorlow RW (1969) End effects and particle migration effects in concentric cylinder rheometry. *Rheol Acta* 8:142–151
- International Organization for Standardization (1993) ISO 3219 Plastics – polymers/resins in the liquid state or as emulsions or dispersions – determination of viscosity using a rotational viscometer with defined shear rate
- ISO/IEC GUIDE 98–3 (2008) [JCGM/WG1/100] Uncertainty of measurement — Part 3: guide to the expression of uncertainty in measurement (GUM:1995)
- Jacob AR, Poulos AS, Kim S, Vermant J, Petekidis G (2015) Convective cage release in model colloidal glasses. *Phys Rev Lett* 115:218301
- Jacob AR, Poulos AS, Semenov AN, Vermant J, Petekidis G (2019) Flow dynamics of concentrated starlike micelles: a superposition rheometry investigation into relaxation mechanisms. *J Rheol* 63:641–653
- Khandavalli S, Hendricks J, Clasen C, Rothstein JP (2016) A comparison of linear and branched wormlike micelles using large amplitude oscillatory shear and orthogonal superposition rheology. *J Rheol* 60:1331–1346
- Kim S, Mewis J, Clasen C, Vermant J (2013) Superposition rheometry of a wormlike micellar fluid. *Rheol Acta* 52:727–740
- Kobayashi H, Nashima T, Okamoto Y, Kaminaga F (1991) End effect in a coaxial cylindrical viscometer. *Rev Sci Instrum* 62:2748–2750
- Krieger IM (1968) Shear rate in the Couette viscometer. *Trans Soc Rheol* 12:5–11
- Krieger IM, Elrod H (1953) Direct determination of the flow curves of non-Newtonian fluids. II shearing rate in the concentric cylinder viscometer. *J Appl Phys* 24:134–136
- Lafarge T, Possolo A (2015) The NIST uncertainty machine. *NCSLI Measure J Meas Sci* 10:20–27. <https://uncertainty.nist.gov>
- Läuger J, Stettin H (2016) Effects of instrument and fluid inertia in oscillatory shear in rotational rheometers. *J Rheol* 60:393–406
- Lin NYC, Ness C, Cates ME, Sun J, Cohen I (2016) Tunable shear thickening in suspensions. *Proc Natl Acad Sci U S A* 113:10774–10778
- Lindsay CH, Fischer EK (1947) End-effect in rotational viscometers. *J Appl Phys* 18:988–996
- Macosko CW (1994) *Rheology: principles, measurements, and applications*. VCH, New York, NY
- Mewis J, Schoukens G (1978) Mechanical spectroscopy of colloidal dispersions. *Faraday Discuss Chem Soc* 65:58–64
- Mewis J, Kaffashi B, Vermant J, Butera RJ (2001) Determining relaxation modes in flowing associative polymers using superposition flows. *Macromolecules* 34:1376–1383
- Moffatt HK (1964) Viscous and resistive eddies near a sharp corner. *J Fluid Mech* 18:1–18
- Moghim E, Vermant J, Petekidis G (2019) Orthogonal superposition rheometry of model colloidal glasses with short-ranged attractions. *J Rheol* 63:533–546
- Philippoff W (1934) *Dynamische Untersuchungen an kolloiden Systemen*. I Grundlagen und Methode. *Phys Z* 35:884–900
- Potantin AA, Shrauti SM, Arnold DW, Lane AM, Mellema J (1997) Testing the structure of magnetic paints with and without superimposed shear. *J Rheol* 41:1337–1347
- Princen HM (1985) Rheology of foams and highly concentrated emulsions. II experimental study of the yield stress and wall effects for concentrated oil-in-water emulsions. *J Colloid Interface Sci* 105:150–171
- Schrag JL (1977) Deviation of velocity gradient profiles from the “gap loading” and “surface loading” limits in dynamic simple shear experiments. *Trans Soc Rheol* 21:399–413
- Simmons JM (1966) A servo-controlled rheometer for measurement of the dynamic modulus of viscoelastic liquids. *J Sci Instrum* 43:887–892
- Simmons JM (1968) Dynamic modulus of polyisobutylene solutions in superposed steady shear flow. *Rheol Acta* 7:184–188
- Smith TL, Ferry JD, Schremp FW (1949) Measurements of the mechanical properties of polymer solutions by electromagnetic transducers. *J Appl Phys* 20:144–153
- Sung SH, Kim S, Hendricks J, Clasen C, Ahn KH (2018) Orthogonal superposition rheometry of colloidal gels: time-shear rate superposition. *Soft Matter* 14:8651–8659
- Tanner RI, Williams G (1971) On the orthogonal superposition of simple shearing and small-strain oscillatory motions. *Rheol Acta* 10:528–538
- van der Vorst B, van den Ende D, Tekin NA, Mellema J (1998) Viscoelastic behavior of an ordering latex suspension in a steady shear flow. *Phys Rev E* 57:3115–3122
- Vermant J, Moldenaers P, Mewis J, Ellis M, Garritano R (1997) Orthogonal superposition measurements using a rheometer equipped with a force rebalanced transducer. *Rev Sci Instrum* 68:4090–4096
- Vermant J, Walker L, Moldenaers P, Mewis J (1998) Orthogonal versus parallel superposition measurements. *J Non-Newtonian Fluid Mech* 79:173–189
- Walker LM, Vermant J, Moldenaers P, Mewis J (2000) Orthogonal and parallel superposition measurements on lyotropic liquid crystalline polymers. *Rheol Acta* 39:26–37
- White CC, Schrag JL (1999) Theoretical predictions for the mechanical response of a model quartz crystal microbalance to two viscoelastic media: a thin sample layer and surrounding bath medium. *J Chem Phys* 111:11192–11206
- Yamamoto M (1971) Rate-dependent relaxation spectra and their determination. *Trans Soc Rheol* 15:331–344
- Yang TMT, Krieger IM (1978) Comparison of methods for calculating shear rates in coaxial viscometers. *J Rheol* 22:413–421
- Zeegers J, van den Ende D, Blom C, Altena EG, Beukema GJ, Mellema J (1995) A sensitive dynamic viscometer for measuring the complex shear modulus in a steady shear flow using the method of orthogonal superposition. *Rheol Acta* 34:606–621

**Publisher's note** Springer Nature remains neutral with regard to jurisdictional claims in published maps and institutional affiliations.